

LES of Premixed Flame Propagation in a Free Straight Vortex

Hannes Kröger · Egon Hassel · Nikolai Kornev ·
Detlef Wendig

Received: 1 September 2008 / Accepted: 20 November 2009 / Published online: 6 January 2010
© Springer Science+Business Media B.V. 2009

Abstract The paper presents experimental and numerical investigations of flame propagation in a free straight vortex which is formed by a movable block swirl generation device. PIV was used to characterize the isothermal flow experimentally and high speed video films were used to gain informations on the flame propagation.

Numerical simulations have been performed using the LES technique. The simulations rely on presumed-PDF combustion modeling with a chemical mechanism reduced by an ILDM approach which has been validated on two test cases.

Numerical and experimental study confirm that the phenomenon of the combustion induced vortex breakdown can take place in an unconfined turbulent vortex with a strong inner axial flow. The LES analysis allowed to determine the main physical mechanisms of this phenomenon.

Keywords Combustion induced vortex breakdown · CIVB · LES · Combustion · Premixed

1 Introduction

Interaction between vortices and flame has attracted attention of specialists for a long time as a problem of fundamental importance for understanding of flame propagation mechanisms in turbulent flows. Vortices enhance the mixing in the diffusion flames (non-premixed) and contribute substantially to the flame propagation. In the premixed combustion, turbulent vortices induce fluctuations increasing the flame propagation speed. The flame propagation speed is governed by chemical processes and turbulence. A long time, generation of turbulent fluctuations was considered as the main mechanism of the vortex-flame interaction. Recently, a new interesting

H. Kröger (✉) · E. Hassel · N. Kornev · D. Wendig
Institute for Technical Thermodynamics,
Albert-Einstein-Str. 2, 18059 Rostock, Germany
e-mail: hannes.kroeger@uni-rostock.de

mechanism of the vortex-flame interaction was observed in the premixed combustion [1, 6, 15, 30]. It has been revealed that the flame can rapidly propagate along the vortices much faster than in surrounding premixed media. This observation can substantially supplement or even change our concepts on mechanisms of flame propagation in turbulent media. Every turbulent flow consists of a collection of vortex filaments of various scales ranging from small hairpin vortices to vortex tubes with scales comparable to the macro scales of the flow. These vortices can play a role of flame conductors increasing the flame propagation speed substantially.

Later, it was found that this phenomenon is not only of pure academic interest, but can take place in various combustion devices. One example is the combustion chamber of gas turbines [10, 11, 23]. Due to progressively more demanding emission limits, stationary gas turbines utilize premixed combustion chambers. The flame in this case is aerodynamically stabilized in a vortex which is forced to break down at a certain location inside the chamber. The practical experience shows that the instabilities in form of flame flashback into the mixing apparatus in front of the combustion chamber may occur and negatively influence the safety of the gas turbine operation.

The aim of the present paper is a study of physical mechanisms governing the flashback in turbulent free vortices.

2 Combustion Induced Vortex Breakdown

Earlier works [10, 14, 30] suggest that the flame flashback in vortices happens after vortex breakdown which is provoked by combustion. The phenomenon was called the combustion induced vortex breakdown (CIVB) and became a subject of extensive investigations. The vortex breakdown may be described as “an abrupt change in the character of a columnar vortex at some axial station. It is usually observed as a sudden widening of the vortex core together with a deceleration of the axial flow and is often followed by a region or regions of recirculation.” [24].

Vortex breakdown was observed first in isothermal flows in tip vortices of delta wings when the angle of attack exceeds a certain threshold. Generally, vortex breakdown appears in positive pressure gradient regions if the swirl of the vortex jet exceeds some critical value which is not universal and depends both on the flow type and the form of the vortex core. In high Reynolds number flows, two different shapes of vortex breakdown are distinguished: the “bubble” type occurs at high swirl intensities while the “spiral” type can be observed at lower swirl intensities.

The bubble type has got its name from the recirculation zone downstream of the stagnation point. Inside this recirculation zone, strong negative axial velocities can be found. The external flow passes the recirculation zone like a solid body, thus it appears like a bubble inside the vortex. During the spiral type vortex breakdown, the axial flow is decelerated as well but the vortex core winds up around the axis. Thus, the spiral type vortex breakdown possesses no axial symmetry whereas the bubble type vortex breakdown is axisymmetric. Depending on the particular flow, transitions from one type into the other may be observed.

Although vortex breakdown is well known for a long time, there is still no general theory for its description. Brown and Lopez [2] have developed an intuitive explanation for the axisymmetric vortex breakdown using kinematic analysis of the

vortex flow. They considered a vortex with an inner axial flow and core diverging along the vortex axis. Because angular momentum is conserved, a fluid particle that is transported radially outward loses circumferential speed. Thus both the trajectory and the streamline corresponding to this particle take spiral form. The same is true for the vorticity lines. The vorticity vectors are reoriented and get a negative circumferential component whenever the streamlines spread radially. According to Biot-Savart's law, vorticity induces a velocity in the whole domain. In the case of an axisymmetric flow, the induced axial velocity at $r = 0$ is related to the circumferential vorticity ω_φ :

$$u_{ind,z} = \frac{1}{2} \int_{-\infty}^{\infty} \int_0^{\infty} \frac{r^2 \omega_\varphi(r, z)}{[r^2 + (z - z')^2]^{\frac{3}{2}}} dr dz \quad (1)$$

From (1), it becomes clear that negative circumferential vorticity causes negative axial velocity at the vortex axis, i.e. the axial flow is decelerated. If the flow on the axis is decelerated, fluid is displaced radially outward by continuity, what in turn causes creation of negative circumferential vorticity. Thus, a feedback loop is created which leads to the breakdown of the axial flow. According to Brown and Lopez [2], the vortex widening is initiated by diffusion effects. They also give a criterion for the occurrence of negative circumferential vorticity: At some initial axial station z_0 , the helix angles of velocity u_φ/u_z have to be larger than those of vorticity $u_\varphi/u_z > \omega_\varphi/\omega_z$.

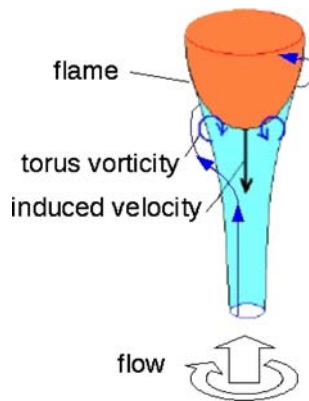
The physics of the vortex breakdown is getting more complicated when the vortex propagates in a combustible media. In [10, 23], it was found that vortex breakdown can be altered or triggered by the presence of a flame. Additional effects caused by combustion can be illustrated using the vorticity transport equation which in inviscid form reads:

$$\frac{\partial \boldsymbol{\omega}}{\partial t} + (\mathbf{u} \cdot \nabla) \boldsymbol{\omega} = \underbrace{-\boldsymbol{\omega} (\nabla \cdot \mathbf{u})}_1 + \underbrace{\frac{1}{\rho^2} \nabla \rho \times \nabla p}_2 + \underbrace{(\boldsymbol{\omega} \cdot \nabla) \mathbf{u}}_3 \quad (2)$$

The three terms on the right hand side are source terms and describe vorticity production by different physical mechanisms. The first term represents vorticity production by density changes, term 2 causes the baroclinic production, i.e. creation of vorticity due to non-parallel isobars and isochors. Finally, term 3 represents vortex stretching. If density is constant, only the latter vorticity production mechanism remains and governs the vortex breakdown in the isothermal case. In this case, the circumferential component of vorticity can only be created by radial expansion of the stream surfaces as predicted in [2]. The combustion case is associated with strong density changes. The circumferential vorticity which is the most important reason for the flow deceleration and the vortex breakdown (see Fig. 1) can be created by two additional physical effects, i.e. by dilution (term 1) and baroclinic (term 2).

Different views on the interaction of flame and vortex breakdown can be found in literature. Ashurst [1] proposes a theoretical model which relies primarily on the baroclinic effect to create the circumferential vorticity. Also, Kiesewetter [19] finds the baroclinic production of vorticity to be dominant in his numerical simulations of Combustion Induced Vortex Breakdown in a gas turbine combustion chamber. Domingo and Vervisch [7] have performed a DNS of a flame interacting with a

Fig. 1 Sketch of vortex/flame interaction during CIVB: The vorticity line (blue) is spiraled, i.e. it gets a circumferential component (torus vorticity). This torus vorticity induces a velocity on the axis (black arrow) that is directed against the initial flow. The deceleration of the flow on the axis may in turn cause a more intense spiraling of the vorticity and thus cause a feedback



vortex. They documented an enhanced flame propagation speed and dominating role of the baroclinic mechanism in the creation of the circumferential vorticity.

Opposedly, Umemura et al. [30] in their model of flame propagation considered only the radial expansion of the vortex tube, which occurs because the flame acts as a volumetric source. In their numerical simulations, they find the pressure

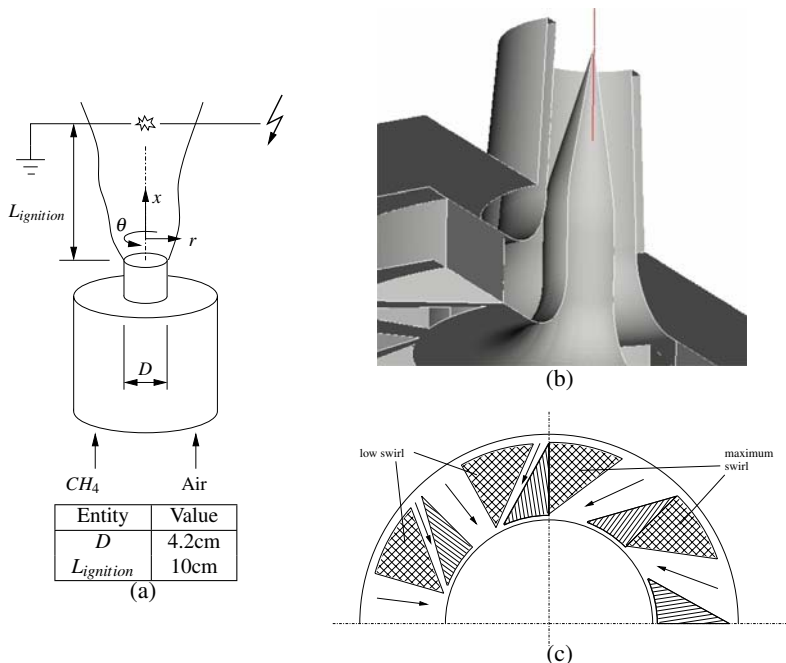


Fig. 2 **a** Experimental setup. The vortex which was generated by the swirl generation device had a positive circumferential velocity component. **b** The nozzle configuration used. **c** Sketch of the movable block swirl principle. The crosshatched blocks are movable along a circular trajectory while the simply hatched blocks are fixed. *Left half* shows block positions for a low swirl configuration, *right half* illustrates the maximum swirl configuration

gradient across the flame surface to be too low for creation of significant amounts of circumferential vorticity.

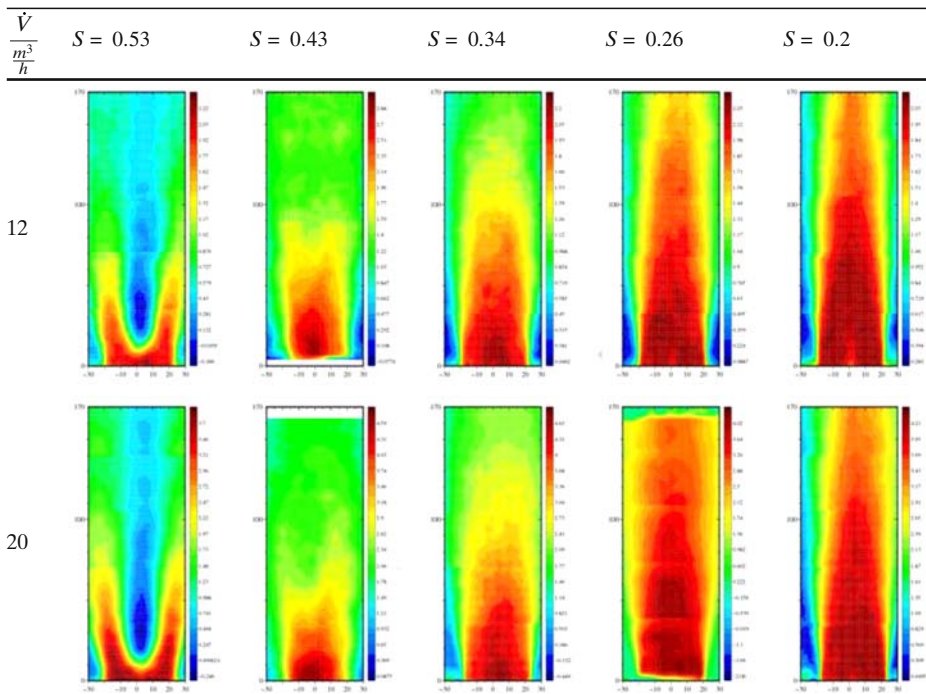
Vortex breakdown changes the velocity field inside of the vortex. Since it is usually accompanied by the creation of stagnation point at the vortex core, the decelerated flow around the stagnation point could allow the flame to propagate upstream or the flame could be even convected upstream by the reversed flow in the recirculation zone. These effects result in the flame flashback as suggested, for instance, by Konle et al. [20] who investigated CIVB in a model gas turbine burner. They documented the flame position downstream of the stagnation point when CIVB occurs.

The aim of the present paper is a study of physical mechanisms governing the flashback in turbulent free vortices with a strong inner axial flow. In contrast to previous works the swirling flow under consideration is unconfined, steady and fully turbulent.

3 Object of Investigation

The flow under study is an unconfined, straight, fully turbulent, steady vortex with an inner strong axial flow. Experimentally, the vortex was generated using the swirl generator device similar to that proposed in [22]. With the help of movable blocks

Table 1 Contour plots of measured mean axial velocity in isothermal flows at different swirl intensities and volume fluxes



inside this device, the swirling intensity of the flow could be adjusted. It is measured by the swirl number S , which is defined by

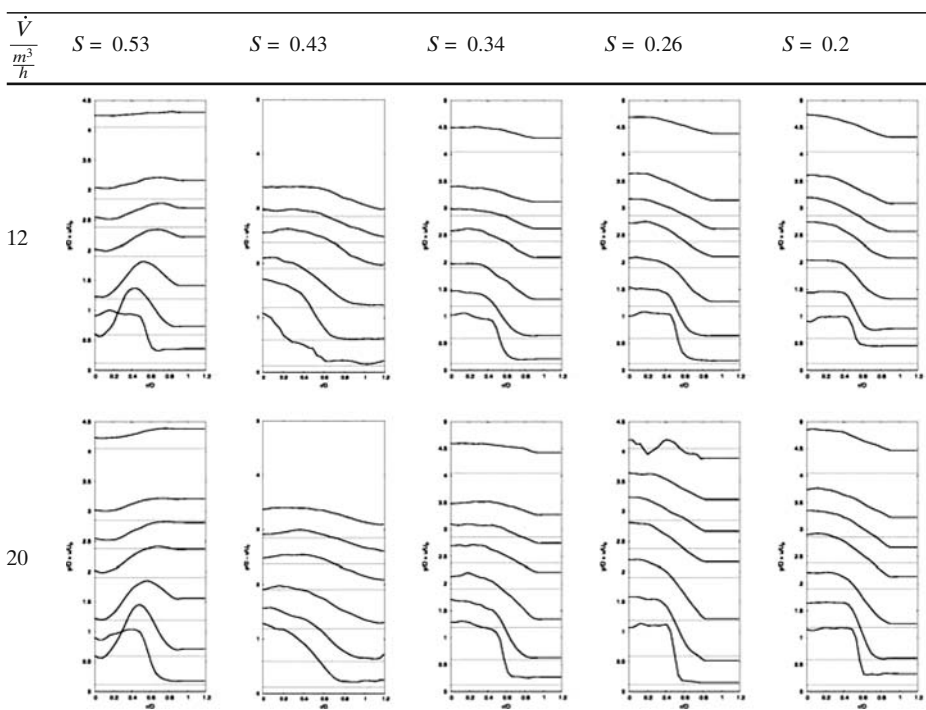
$$S = \frac{\dot{D}}{\dot{I} R_{ref}} \quad \text{with} \quad \dot{D} = \int_0^R 2\pi \rho u_{tan} u_{ax} r^2 dr \quad \dot{I} = \int_0^R 2\pi \rho u_{ax}^2 r dr \quad (3)$$

where R_{ref} is a reference radius and the integral is over some reference plane, which is orthogonal to the vortex axis, e.g. the nozzle exit plane of the swirl generator device. The swirl number S of the applied device could be selected between $S = 0$ and $S = 2.3$.

The jet consisted of a mixture of methane and air with a selectable equivalence ratio Φ and was ejected into the ambient surrounding air.

Contrary to the configuration in [22], the form of the swirler nozzle and the method of ignition was changed. In the previous study, a nozzle with a cylindrical bluff body was used, whereas in the current study, a conical inset instead of the bluff body was applied (see Fig. 2b). Thus, the formation of a recirculation zone and a wake behind the bluff body was avoided. The axial velocities in the wake could drop below the turbulent flame speed and thus conceivably allow the flame to propagate towards the nozzle even without flame acceleration by Combustion Induced Vortex Breakdown. By this, a possible misinterpretation of such an event as CIVB is avoided.

Table 2 Profiles of measured mean axial velocity in isothermal flows at different swirl intensities and volume fluxes



Furthermore, the flame was ignited by an electric spark to improve the comparability between experimental and simulated flashbacks. Previously, a stationary flame at a ring burner was used as ignition source in experiments. To simulate the flashback initiation, simulation of the transition from the stationary flame to the propagating flame was required with a properly modeled stationary flame as prerequisite. This introduces further uncertainties which were avoided in the current work by starting the flashback with an explicit event like an electric spark. In the remainder of this work, only spark-initiated flashback events are considered, with the spark location set to $2.4d_n$ (10cm) above the nozzle onto the centerline.

The flame propagation is recorded by high speed video films.

4 Experimental Observations

The isothermal flow fields have been measured using PIV for different values of the swirl number S and volume flux \dot{V} through the swirl generator. Especially interesting is the axial velocity. Contour plots of the axial velocity are shown in Table 1 and selected profiles of axial velocity are shown in Table 2. It can be recognized that vortex breakdown in the isothermal flow begins to occur above a swirl number of $S > 0.43$. A strong deceleration of the flow can be observed at $S = 0.47$ and reversal of the axial velocity has occurred at $S = 0.53$.

Table 3 Contour plots of measured axial velocity RMS in isothermal flows at different swirl intensities and volume fluxes

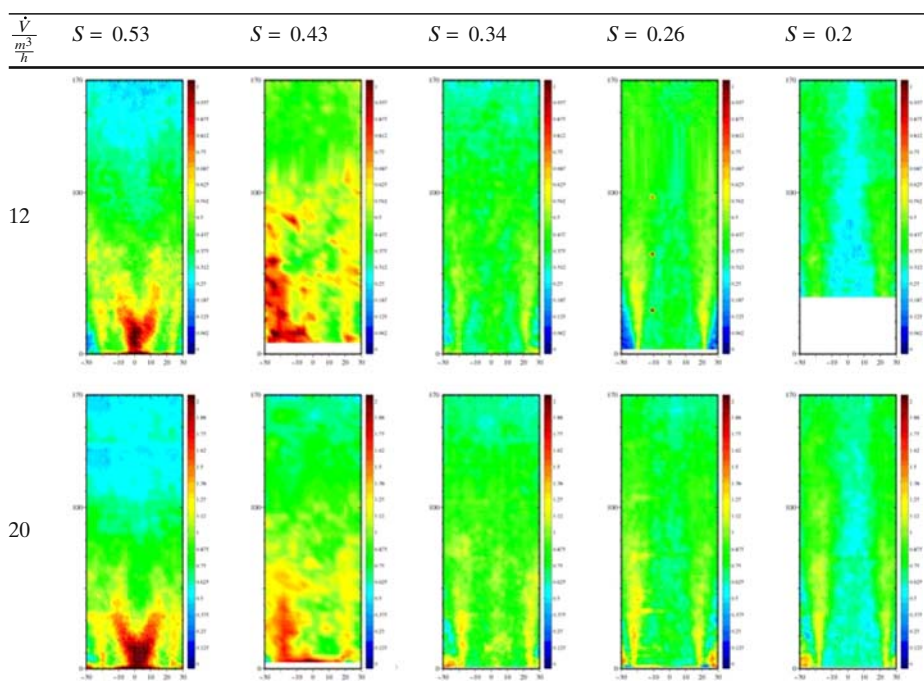
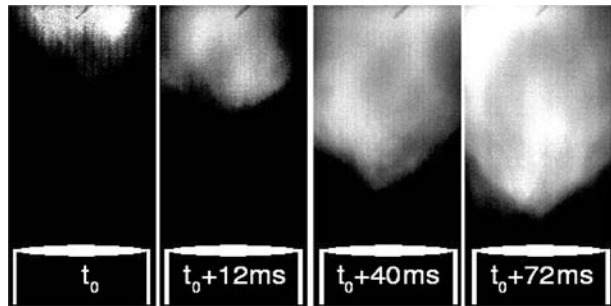


Fig. 3 Sequence of images from high speed video film of case 9V20



If a flame is ignited above the swirl generator nozzle at a swirl number below $S \leq 0.43$ one could expect that it would be blown downstream, because the flow velocities everywhere exceed the turbulent flame speed. The simplest approximation for the turbulent flame speed is:

$$s_T = s_L + u' \quad (4)$$

Measurements show, that velocity RMS is approximately $u' \approx 1\text{m/s}$ for $\dot{V} = 20\text{m}^3/\text{h}$ and $u' \approx 0.5\text{m/s}$ for $\dot{V} = 12\text{m}^3/\text{h}$ (see Table 3). The laminar flame speed is maximum for a slightly lean mixture. For methane/air $s_{L,max}(\Phi = 1.15) = 0.42\text{m/s}$ (e.g. [13]). From this estimations, it follows that an upper limit for the turbulent flame speed in the current case is $s_T(\dot{V} = 12\text{m}^3/\text{h}) < 0.92\text{m/s}$ and $s_T(\dot{V} = 20\text{m}^3/\text{h}) < 1.42\text{m/s}$.

With the investigated setup (ignition height $2.4d_n$) the flame was either blown downstream or a flashback occurred. A steady flame could not be realized. Flame flashbacks begin to occur when $S \geq 0.34$ (if $\dot{V} = 12\text{m}^3/\text{h}$) and $S \geq 0.43$ (if $\dot{V} = 20\text{m}^3/\text{h}$) respectively. At that conditions, the mean axial velocities still exceed the turbulent flame speed by 80% ($12\text{m}^3/\text{h}$) and 60% ($20\text{m}^3/\text{h}$). But despite this, flame propagation with a velocity $v_f \approx 0.33\text{m/s}$ ($12\text{m}^3/\text{h}$) and $v_f \approx 1\text{m/s}$ ($20\text{m}^3/\text{h}$) towards the nozzle was observed in measurements.

A sequence of images from a high speed video film of a flashback event is shown in Fig. 3. The flame shows a conical shape, which indicates that the accelerating mechanism acts at the vortex core. This agrees with the hypothesis, that CIVB is accelerating the flame propagation.

5 Numerical Method

5.1 Concept and implementation

Since only integral parameters of the flashback event could be retrieved from experiments, numerical simulations were performed to get a deeper insight into the flow physics. The large eddy simulation (LES) technique was applied since it is expected to be generally more accurate and requires less modeling effort than unsteady Reynolds-Averaged Navier-Stokes (URANS) based techniques.

All simulations presented subsequently were carried out using the open source PDE solution framework OpenFOAM [34]. The standard version of OpenFOAM contains only one combustion model for premixed and partially premixed combus-

tion which is the Weller b- Ξ model [32, 33]. This model was applied in our previous work [22]. Further testing of this model did not reveal satisfactory results for all test cases. Moreover, application of this model was connected with problems of numerical instability. Therefore in the current work, a presumed-PDF model based on ILDM reduced chemistry was applied instead.

In the presumed-PDF LES solver, the spatially favre filtered Navier-Stokes equations are solved:

$$\frac{\partial \bar{\rho}}{\partial t} + \nabla \cdot (\bar{\rho} \tilde{\mathbf{u}}) = 0 \quad (5)$$

$$\begin{aligned} \frac{\partial (\bar{\rho} \tilde{\mathbf{u}})}{\partial t} + \nabla \cdot (\bar{\rho} \tilde{\mathbf{u}} \tilde{\mathbf{u}}) = & \nabla \cdot [\mu (\nabla \tilde{\mathbf{u}} + (\nabla \tilde{\mathbf{u}})^T)] - \frac{2}{3} \nabla [\mu \nabla \cdot \tilde{\mathbf{u}}] \\ & - \nabla \bar{p} + \rho \tilde{\mathbf{g}} - \nabla \cdot (\bar{\rho} \tau_{SGS}) \end{aligned} \quad (6)$$

The unclosed stress term $\tau_{SGS} = \tilde{\mathbf{u}}\tilde{\mathbf{u}} - \tilde{\mathbf{u}}\tilde{\mathbf{u}}$ appears in these equations due to the spatial filtering and requires a closure model. In all performed simulations, a closure model based on the eddy viscosity approach

$$\mu_t = \rho C_k \sqrt{k_{SGS}} \Delta \quad (7)$$

was applied. A transport equation was solved for the residual energy k_{SGS} :

$$\begin{aligned} \frac{\partial \bar{\rho} k_{SGS}}{\partial t} + \nabla \cdot (\bar{\rho} \tilde{\mathbf{u}} k_{SGS}) = & \nabla \cdot [(\mu + \mu_t) \nabla k_{SGS}] + 2\mu_t \nabla \tilde{\mathbf{u}} \cdot \left[(\nabla \tilde{\mathbf{u}} + \nabla \tilde{\mathbf{u}}^T) - \frac{1}{3} \nabla \cdot \tilde{\mathbf{u}} \mathbf{I} \right] \\ & - \frac{2}{3} \bar{\rho} k_{SGS} \nabla \cdot \tilde{\mathbf{u}} - C_e \bar{\rho} \frac{k^{\frac{3}{2}}}{\Delta} \end{aligned} \quad (8)$$

The equation system is solved using the PISO scheme for reacting flows [18].

Chemical reactions and combustion involve conversion of one chemical species into another. Thus, for the mass of each species i , individual transport equations are written. After applying the LES filter, they read:

$$\frac{\partial (\bar{\rho} \tilde{Y}_i)}{\partial t} + \nabla \cdot (\bar{\rho} \tilde{Y}_i \tilde{\mathbf{u}}) = \nabla \cdot (\bar{\rho} D \nabla \tilde{Y}_i) + \tilde{\omega}_i - \bar{\rho} F_{SGS,i} \quad (9)$$

Again, due to the filtering of the nonlinear convection term, an unclosed flux term $F_{SGS,i} = \tilde{Y}_i \tilde{\mathbf{u}} - \tilde{Y}_i \tilde{\mathbf{u}}$ appears for which a closure model is required. In the following simulations, this term is closed by a gradient assumption

$$F_{SGS,i} = -\frac{\mu_t}{Sc_t} \nabla Y_i \quad (10)$$

with the turbulent Schmidt number generally set to $Sc_t = 1$. Although counter gradient diffusion occurs especially in premixed combustion this is not incorporated here. That is mainly because no proper models are available for counter gradient diffusion. Modeling it would require a turbulent flux model of higher order, i.e. solution of a transport equation for $F_{SGS,i}$. This would introduce new closure models and sources of errors. Despite this, the error in neglecting counter gradient diffusion in $F_{SGS,i}$ is bounded by the fact that it is at least partially resolved in LES through the resolved turbulent motion, even when gradient diffusion SGS models are used [29].

Additionally, the source term appears spatially filtered in (9). Modeling of the filter operation on this source term is the big challenge in combustion simulation.

One possible approach, which is used in the current work, is to presume the shape of the probability density function (PDF) of the quantities on which ω_i depends. In a general chemical system, the net production rate of each species may depend on all n species in the system and on temperature:

$$\bar{\omega}_i = \int_0^1 \int_0^1 \dots \int_0^1 \int_0^\infty \omega_i(Y_1, Y_2, \dots, Y_n, T) P(Y_1, Y_2, \dots, Y_n, T) dY_1 dY_2 \dots dY_n dT \quad (11)$$

Thus, a joint PDF $P(Y_1, Y_2, \dots, Y_n, T)$ of all defining quantities needs to be presumed, which is difficult for small chemical mechanisms and almost impossible for realistic mechanisms, like for example GRI3.0 for natural gas combustion [9], which contains 52 species. One common approach is to neglect all correlations between the stochastic quantities and assume statistical independence $P(Y_1, Y_2, \dots, Y_n, T) = P_1(Y_1) \cdot P_2(Y_2) \cdot \dots \cdot P_n(Y_n) \cdot P_T(T)$ which is probably hard to justify in the general case.

It is therefore only worth to use the presumed PDF approach with reduced mechanisms. The best adapted methods for reducing the chemical mechanisms are based on finding automatically intrinsic low-dimensional manifolds in the chemical state space [26]. Depending on the required temporal resolution of the system dynamics, one, two or three dimensional manifolds are usually sufficient to describe the thermophysical state of the system. That means that instead for all n species mass fractions only equations for one to three almost arbitrarily chosen progress variables are needed to be solved. These progress variables are usually mass fractions of selected species or linear combinations of them. The only requirement is that a unique mapping from the progress variable to the low-dimensional manifold is possible.

Different methods for finding the low-dimensional manifolds have been proposed. In their pioneer work [26], Maas and Pope used an eigenspace analysis of the chemical source terms to find the manifolds. Unfortunately, this approach does only work well in the regions of the chemical state space where the chemistry is fast and approximations are needed to extend the manifolds towards the unburnt and slowly reacting states. These are for example linear prolongation or flamelet prolonged manifolds (FPI) [8]. Recently, Maas and Bykov have developed a novel approach for computing the manifolds by solving a partial differential equation [25]. The resulting manifolds are named reaction diffusion manifolds (REDIM) because the diffusion is also taken into account. Similar to FPI is the extraction of manifolds from flamelets (flamelet generated manifolds, FGM) [31]. In this method, the fact is used, that all states in a laminar premixed flame belong to a one-dimensional attracting manifold in state space, that connects the unburnt state with the equilibrium point and includes diffusion as well. After computation of a laminar flame and selection of an appropriate progress variable, the thermophysical states and reaction rates can be tabulated.

In the current work, the latter FGM method has been used, because of its easy implementation. The flamelets have been computed using CANTERA [12] and stored in a database. As progress variable, the mass fraction of CO_2 was selected. Because the combustion regime in the described experimental setup is partially premixed, the mixture fraction had to be included in the chemistry table as a coordinate as well. The table is then generated from a number of flamelet calculations with different mixture

fractions. At too lean mixtures, where the flamelet calculation does not converge any more, the table is filled by interpolating between the leanest computed flamelet and pure air.

Finally, the scalar equations, that had to be solved with the reduced system, are:

$$\frac{\partial(\bar{\rho}\tilde{Y})}{\partial t} + \nabla \cdot (\bar{\rho}\tilde{Y}\tilde{\mathbf{u}}) = \nabla \cdot \left[\bar{\rho} \left(D + \frac{\mu_t}{Sc_t} \right) \nabla \tilde{Y} \right] + \bar{\omega} \quad (12)$$

$$\frac{\partial(\bar{\rho}\tilde{Z})}{\partial t} + \nabla \cdot (\bar{\rho}\tilde{Z}\tilde{\mathbf{u}}) = \nabla \cdot \left[\bar{\rho} \left(D + \frac{\mu_t}{Sc_t} \right) \nabla \tilde{Z} \right] \quad (13)$$

where Y is the progress variable $Y = Y_{CO_2}$. The properties of the mixture then can be retrieved from the chemistry table:

$$\rho = \rho(Y, Z) \quad (14)$$

$$\lambda = \lambda(Y, Z) \quad (15)$$

$$c_p = c_p(Y, Z) \quad (16)$$

$$T = T(Y, Z) \quad (17)$$

$$\omega = \omega(Y, Z) \quad (18)$$

It now remains to close the chemical source term in (12). As mentioned before, this was done by application of a presumed-PDF for the defining variables. The PDF is presumed to be an adequate mathematical function, e.g. the beta-distribution, that contains free parameters. These parameters are determined from the moments of the stochastic quantities, i.e. the mean and variance. Furthermore, a joint PDF is needed for Y and Z . This is approximated by assuming statistical independence of the two variables and neglecting correlations between them. The sought filtered source term $\bar{\omega}$ then becomes a function of the filtered progress variable \tilde{Y} and mixture fraction \tilde{Z} and their variances $Y_v = \widetilde{Y^2} - \tilde{Y}\tilde{Y}$, $Z_v = \widetilde{Z^2} - \tilde{Z}\tilde{Z}$:

$$\bar{\omega}(\tilde{Y}, Y_v, \tilde{Z}, Z_v) = \int_0^1 \int_0^1 \omega(Y, Z) P_Y(Y, \tilde{Y}, Y_v) P_Z(Z, \tilde{Z}, Z_v) dY dZ \quad (19)$$

This integration is carried out as a preprocessing step before the actual simulation. A four-dimensional lookup table is created, such that for every realizable value of \tilde{Y} , Y_v , \tilde{Z} , Z_v the properties of the thermophysical state can be interpolated:

$$\bar{\rho} = \bar{\rho}(\tilde{Y}, Y_v, \tilde{Z}, Z_v) \quad (20)$$

$$\bar{\lambda} = \bar{\lambda}(\tilde{Y}, Y_v, \tilde{Z}, Z_v) \quad (21)$$

$$\bar{c}_p = \bar{c}_p(\tilde{Y}, Y_v, \tilde{Z}, Z_v) \quad (22)$$

$$\bar{T} = \bar{T}(\tilde{Y}, Y_v, \tilde{Z}, Z_v) \quad (23)$$

$$\bar{\omega} = \bar{\omega}(\tilde{Y}, Y_v, \tilde{Z}, Z_v) \quad (24)$$

To compute the variance of the controlling variables, transport equations for their second moments $\widetilde{Y^2}$, $\widetilde{Z^2}$ are solved:

$$\frac{\partial(\bar{\rho}\widetilde{Y^2})}{\partial t} + \nabla \cdot (\bar{\rho}\widetilde{\mathbf{u}}\widetilde{Y^2}) = \nabla \cdot \left[\bar{\rho} \left(D + \frac{\mu_t}{Sc_t} \right) \nabla \widetilde{Y^2} \right] - 2\bar{\rho}\widetilde{\chi}_Y + 2\bar{\rho}\widetilde{\omega}Y \quad (25)$$

$$\frac{\partial(\bar{\rho}\widetilde{Z^2})}{\partial t} + \nabla \cdot (\bar{\rho}\widetilde{\mathbf{u}}\widetilde{Z^2}) = \nabla \cdot \left[\bar{\rho} \left(D + \frac{\mu_t}{Sc_t} \right) \nabla \widetilde{Z^2} \right] - 2\bar{\rho}\widetilde{\chi}_Z \quad (26)$$

The source term in (25) is preintegrated as well and included in the lookup table. The scalar dissipation rate $\widetilde{\chi}_\phi$ of $\phi = (Y, Z)$ is modeled by a linear relaxation hypothesis:

$$\bar{\rho}\widetilde{\chi}_\phi = \overline{\rho D |\nabla \phi|^2} = \bar{\rho} D |\nabla \widetilde{\phi}|^2 + C_D \frac{\mu_t}{Sc_t} \frac{\widetilde{\phi^2} - \widetilde{\phi}^2}{\Delta^2} \quad (27)$$

6 Validation of the PDF Combustion Model

To demonstrate the ability of the implemented presumed-PDF model for correctly reproducing the turbulent flame speed in a premixed and partially premixed case and check for a grid-dependency, results for two test cases will be presented subsequently.

The first test case is a turbulent combustion bomb. It is characterized by a rather simple flow field, but main features of turbulent combustion are present: turbulence-flame interaction, flame wrinkling and gas expansion. The second test case is a turbulent bunsen flame with air entrainment. It shall demonstrate the validity of the combustion model in a partially premixed context.

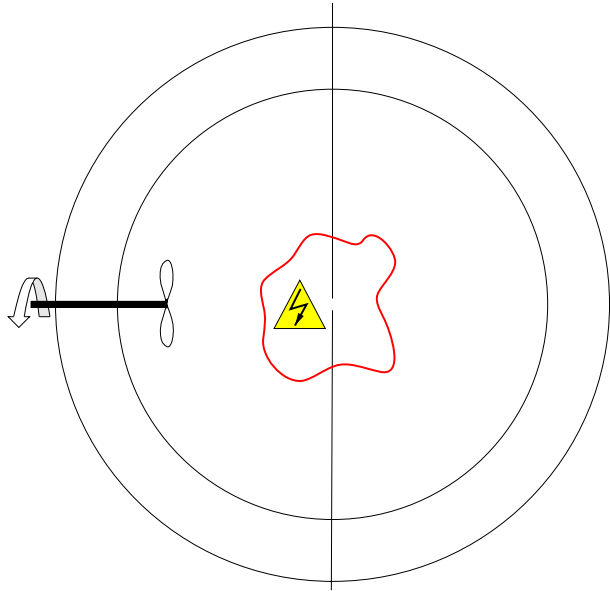
6.1 Premixed turbulent combustion bomb

A sketch of the experimental setup of a combustion bomb is shown in Fig. 4. The bomb initially contains a well defined, homogeneous mixture of fuel and air. The turbulence is generated by stirring the charge with a fan. Finally, the mixture is ignited in the center by an electrical spark. After ignition, the flame front spreads spherically through the volume, thereby interacts with the turbulence and gets wrinkled.

The results in this chapter are compared to experimental data from Nwagwe et al. [27]. In that work, the temporal evolution of the flame kernel radius was measured. The flame radius is extracted by processing images of high speed schlieren films. To define the initial conditions, Ref. [27] gives velocity RMS and integral length scale, which were obtained from LDV measurements.

In the simulations, the domain was chosen to be a cube, much smaller than the entire volume of the combustion bomb in [27] and the simulations were only carried up to a point where a small fraction of the charge was burned. This was done to avoid a significant pressure rise and to remove the necessity of taking compressibility into account.

Grids at different refinement levels were used. A coarse one with a resolution of 31^3 cells, finer ones with 64^3 and 128^3 cells and a very fine grid with 256^3 cells. From a laminar flame calculation with the complete chemical mechanism GRI3.0 [9], a flame thickness of $\delta_L^0 = 0.33\text{mm}$ was computed for the present case. The ratios of cell edge

Fig. 4 Sketch of a turbulent combustion bomb

length to laminar flame thickness are given in Table 4, they are $\Delta/\delta_L^0 = 19.4, 9.4, 4.7$ and 2.35, respectively.

The initial turbulence was generated by the method of turbulent spots [21]. The computational domain was filled up with vortons, that induced divergence free turbulent fluctuations. The inner distribution of these spots was chosen according to homogeneous turbulence with an energy spectrum $E(k) \propto k^{-5/3}$. It was possible to directly prescribe the integral length scale, since it is connected to the spot size. The RMS was imposed by properly scaling the turbulent fluctuations.

No attempt has been made to model the ignition process in detail. Artificial source terms were inserted into the progress variable equation to initiate the combustion. The strength, duration and time profile of the source term was chosen by trial and error. The main problem here was to ensure that the combustion process sustained after removing the source term and to avoid numerical instabilities that occurred when the source term was too strong or the ignition region too large. Despite this, there was no noticeable effect of the source term parameters on the final result.

Table 4 Simulations of the turbulent combustion bomb: Computed variants and common parameters

Label	Grid	Δ/δ_L^0	$\sqrt{\langle u^2 \rangle}/\text{ms}^{-1}$	Parameter	Value
Plow	31^3	19.4	2.36	Mixture	Propane/Air
Phigh1	64^3	9.4	2.36	Equivalence ratio	$\Phi = 1$
Phigh2	128^3	4.7	2.36	Initial temperature	$T_{\text{initial}} = 300\text{K}$
Phigh3	256^3	2.35	2.36	Initial pressure	$p_{\text{initial}} = 1\text{bar}$
IPhigh1	64^3	9.4	4.72	Integral length scale	$L = 20\text{mm}$
IPhigh2	128^3	4.7	4.72	Domain cube length	$h = 0.2\text{m}$

Among all examined cases in [27], only two were selected for validation: these that utilized propane as fuel at atmospheric initial pressure. Two different turbulence intensities have been investigated. The parameters are summarized in Table 4.

The result of the simulations are plots of the flame kernel diameter versus time shown in Fig. 5. It has been decided to compare these results directly to the plots of flame radius vs. time from [27] rather than performing a regression analysis and report flame speeds because the former is the primary result of the experiment as well as of the simulations. Furthermore, the experiments as well as the simulations reproduce and agree well in the initial transient phase between ignition and constant speed flame propagation which is recognizable in these plots.

The simulation results have been evaluated by summing up the volume of all grid cells with a temperature $T > 1000\text{K}$. This volume was equated with that of a sphere and the mean flame radius was the radius of that sphere.

For the case with low turbulence intensity, the experimental flame speeds are good reproduced provided that the grid resolution is fine enough. The simulations also show the increase of the burning rate in the early stage of the flame propagation and its convergence to a steady state later on. There are deviations between the curves at ignition because all LES flames start at a diameter of approximately 5mm .

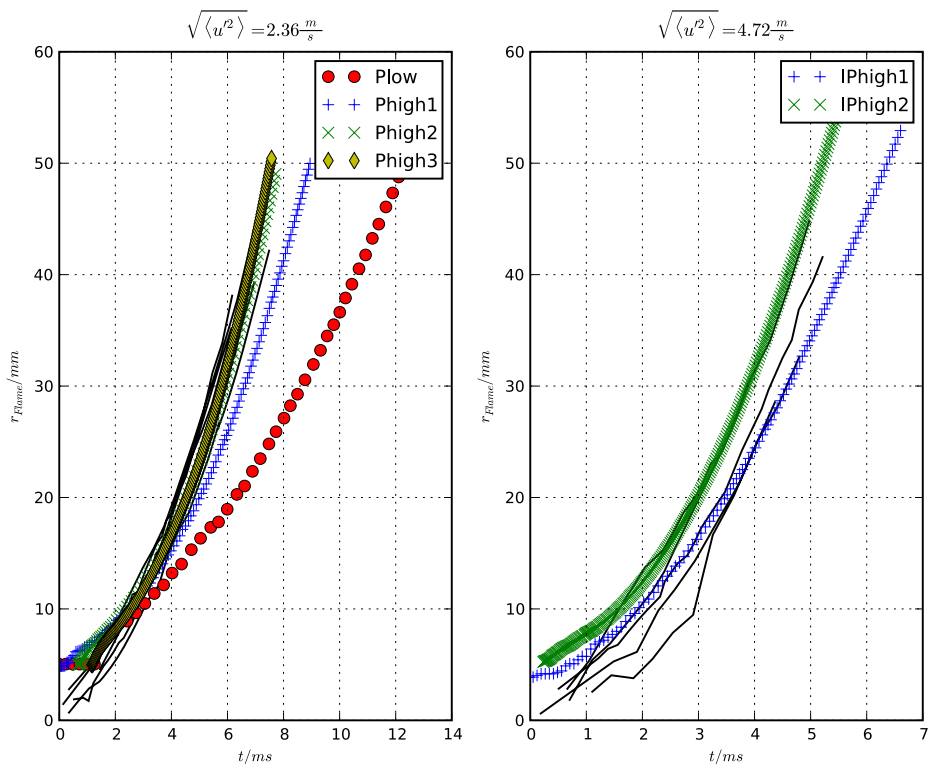


Fig. 5 Development of flame kernel diameter in LES of turbulent combustion bomb. The *black solid lines* show multiple experimental runs at the same initial conditions and give an impression of the experimental repeatability

This corresponds to the edge length of a grid cell on the coarsest grid and was the minimum flame radius that could appear since the size of the ignition zone was kept constant throughout all simulations. The grid with the coarsest resolution $\Delta/\delta_L^0 = 19.4$ does not give satisfactory results. But for more increased resolutions, a convergence towards the measurement can be recognized, as it has to occur for every reasonable numerical model.

To assess the ability of the combustion model to reproduce the interaction of the flame with turbulence, simulations at a higher turbulence intensity have been performed as well. The experimental data for this case shows more scatter, especially in the early stage of flame development. Nevertheless, all experimental runs end up with the same steady propagation speed, which agrees very well with that of the numerical simulations. The effect of higher turbulence intensity, i.e. an acceleration of the flame, is thus correctly reproduced.

6.2 Bunsen flame

The Bunsen flame is a common object for model validation and has been experimentally investigated by many researchers in different variations. This test case is included here, because it has some similar features as the CIVB case described above: the combustion is essentially premixed but entrainment of air occurs from the surrounding. Thus, a partially premixed formulation of the combustion model is required.

For the current test, the Bunsen flame of Chen et al. [5] was selected. This experiment was developed within the JOULE project at RWTH Aachen for validation of combustion models. All data is available on the website [4] of the Institute for Combustion Technology. It has been used for validation e.g. by Hoffmann [17], Herrmann [16] and Pitsch et al. [28]. From the different flame configurations that have been investigated by Chen, only the configuration F2 has been simulated. A sketch of the experimental setup is shown in Fig. 6. It consists of a central jet which is ejected by a nozzle with a diameter of $D = 12\text{mm}$. The flame is stabilized by a pilot flame that burns on a perforated plate with a diameter of $D_{\text{coflow}} = 68\text{mm}$. The burner was operated with methane as fuel and both streams had the same composition $\Phi = 1$.

From the chemical and physical time and length scales which are given in [5] it follows for the ratio of integral length scale of turbulence to the flame thickness $L/\delta_L^0 = 13.7$ and for the ratio of velocity RMS to laminar flame speed $u'/s_L^0 = 3.7$. The flame is therefore located well within the thin reaction zone regime.

The computational domain was cylindrical with a diameter of $24D$ and a length of $33D$. The grid had a block-structured topology and consisted of approximately 700 000 hexahedral cells. By grading the resolution along the block edges, a LES filter width of $\sim 0.3\text{mm}$ could be achieved around the centerline. In the transition region between core jet and coflow the filter width raises to $\sim 0.7\text{mm}$ and is $\sim 1\text{mm}$ in the coflow region.

At the central jet inlet, a mean velocity profile according to the measurements was prescribed. Turbulent velocity fluctuations were superimposed and generated by the turbulent spot method [21]. The coflow velocity was very slow compared to the central jet. A constant mean velocity of $U_{\text{coflow}} = 1.5\text{m/s}$ was prescribed. Special care was required to set up the lateral boundaries, because air entrainment was possible

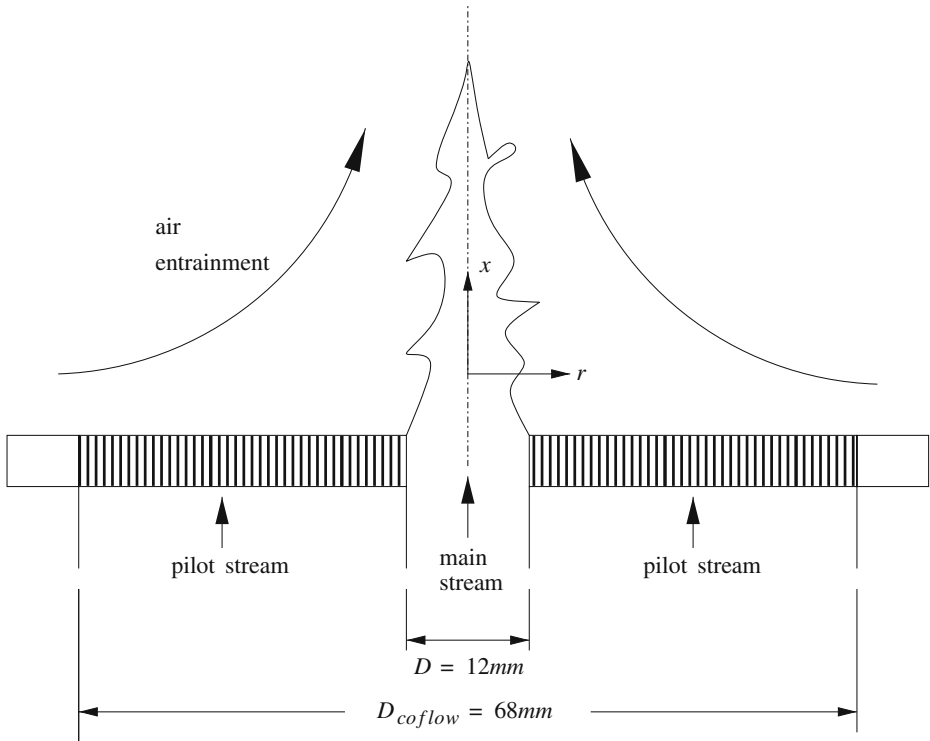


Fig. 6 Sketch of the Bunsen flame setup

across this surfaces. This was treated by specifying the total pressure p_{tot} . When entrainment occurs, the static pressure at the boundary was calculated according to the Bernoulli equation from the total pressure and the entrainment velocity

$$p = p_{tot} - \frac{\rho}{2} u_{in}^2 \quad (28)$$

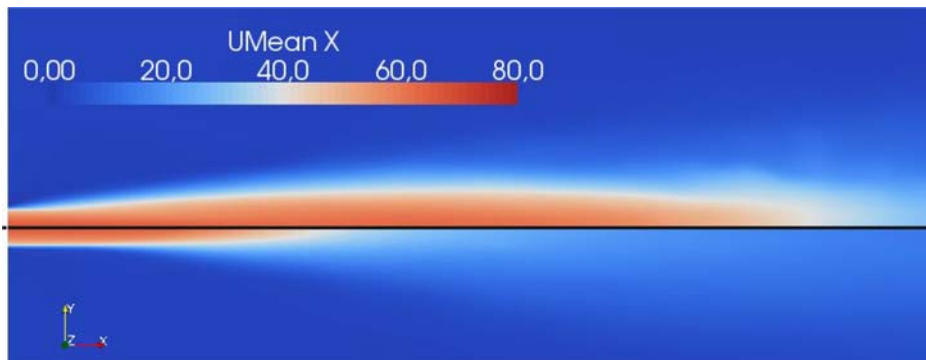


Fig. 7 Time averaged fields of axial velocity. The lower half shows the isothermal case, the upper half the reacting flow

For validation, the time averaged streamwise velocity, the turbulent kinetic energy, the mean temperature and its RMS were available. Figure 7 shows contour plots of the axial velocity field in the isothermal and the reacting flow. The isothermal and reacting fields are clearly distinct because of the gas expansion due to combustion which accelerates the flow. The agreement between the numerical simulations and the measurements is good. Profiles of velocity at different heights above the nozzle are shown in Fig. 8. The experimental curves for the reacting case show a plateau near the axis around $r/D \approx 0$ which looks like problems in the measurements but is not commented in the literature. The plots also show profiles of the turbulent kinetic energy for the reacting flow case which is also in good agreement.

The flame in the Bunsen burner is conically shaped and the cone aperture angle and thus the cone length is related to the central nozzle's exit velocity v_u and the turbulent flame speed s_T :

$$\frac{s_T}{v_u} = \sin \theta \quad (29)$$

According to [5], the instantaneous flame height H_c/D is 10.5. It is defined as the height above the burner, where most of the fuel is consumed. After time averaging the numerical results, this height was found to be approximately $H/D = 9.5$, which is slightly too short but still in good agreement with the measured one. This shows

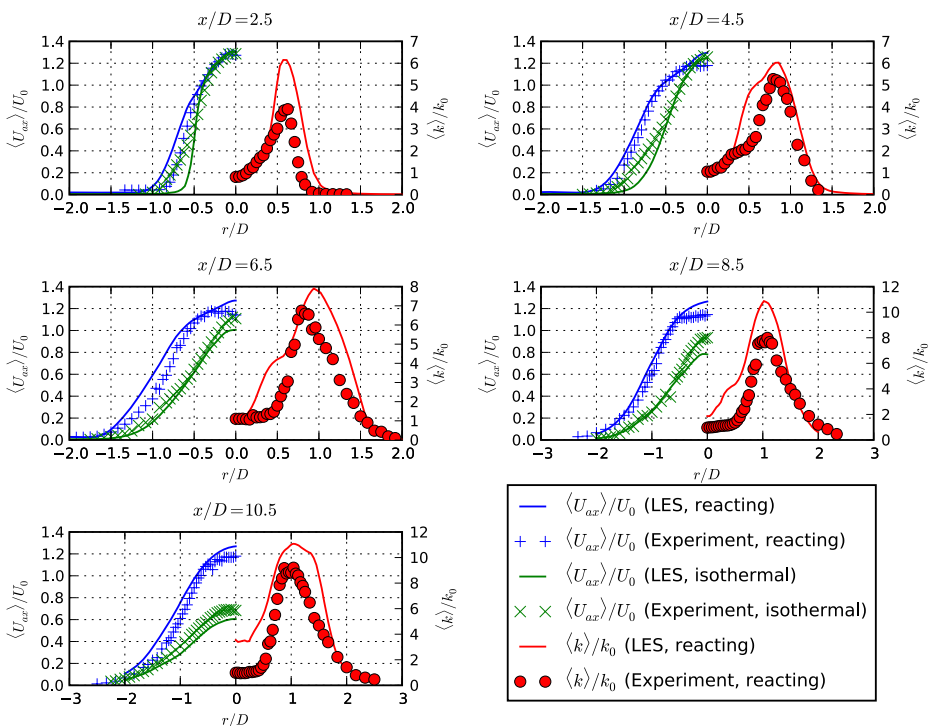


Fig. 8 Mean velocity profiles in Bunsen flame test case. Experimental data: [4]

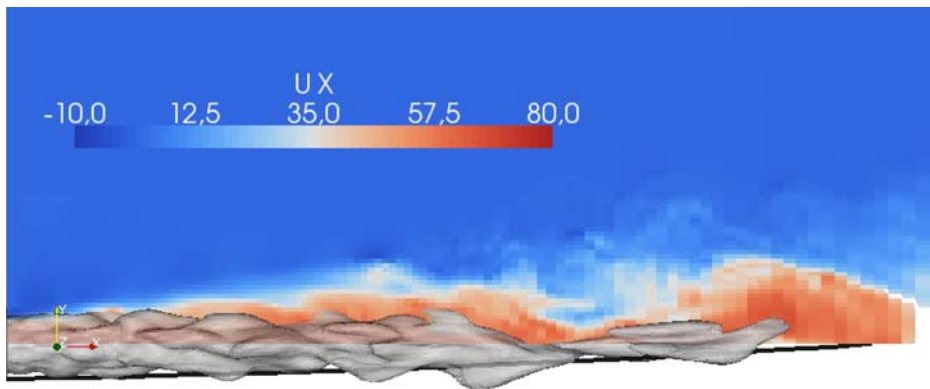


Fig. 9 Instantaneous flame surface. The thick black line shows the time averaged flame contour from [5]

that the simulation reasonably predicts the turbulent flame speed. Figure 9 shows an example of the flame surface and the axial velocity field at some time instance.

Finally, plots of the mean temperature and temperature RMS are shown in Fig. 10. At the lower positions next to the nozzle, the maxima of the numerically computed temperatures are too high. This can be attributed to the assumption of an adiabatic

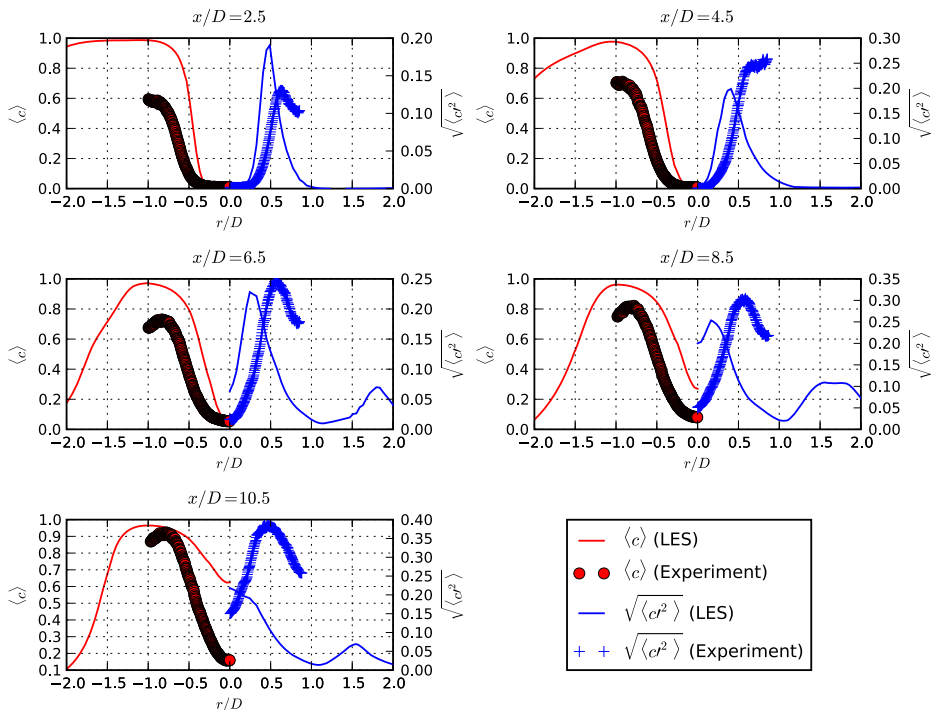


Fig. 10 Mean temperature profiles in Bunsen flame test case. Experimental data: [4]

flow which was used here. From the lowest profile at $x/D = 2.5$, it is obvious that due to the heat losses at the perforated pilot burner plate, the maximum temperature reaches only 60% of the adiabatic flame temperature. The temperature maxima are captured better further downstream because heat losses decrease and the influence of entrainment increases there.

Concluding, the model seems to perform well for this partially premixed combustion case.

7 Numerical Model

The domain for the numerical simulation of the flame flashback had a cylindrical shape with a diameter of $6.66d_n$ and length in axial direction of $4.7d_n$. The computational domain of the combustion simulations did not include the interior of the swirl generator device. Instead, the domain began at the nozzle exit plane and the velocity profile was prescribed there. The mesh was purely hexahedral with a block structured layout. The mesh contained about 600 000 cells and the filter width in the interesting region was about $\Delta \approx 1\text{ mm}$ (where $\Delta = \sqrt[3]{V_{\text{cell}}}$). Slices through the grid are shown in Fig. 11.

Since turbulent fluctuations are partly resolved in Large Eddy Simulation, it is also required to prescribe turbulent fluctuations at the inflow boundaries. Therefore, the method of turbulent spots [21] was used. The mean velocity profiles were gained from auxiliary simulations of the swirl generator device and checked against experimental measurements of the isothermal flow. For the method of turbulent spots, velocity RMS and length scales or autocorrelation functions are required as input. In this case, the RMS and length scales were also gained from experimental data.

It turned out, that it was necessary to apply non-reflecting boundary conditions for pressure at the lateral and outflow boundaries. Since the code is compressible, pressure waves appear at the ignition point during ignition and propagate through the computational domain. The non-reflecting boundary condition allows them to leave the domain without influencing the flow field upstream.

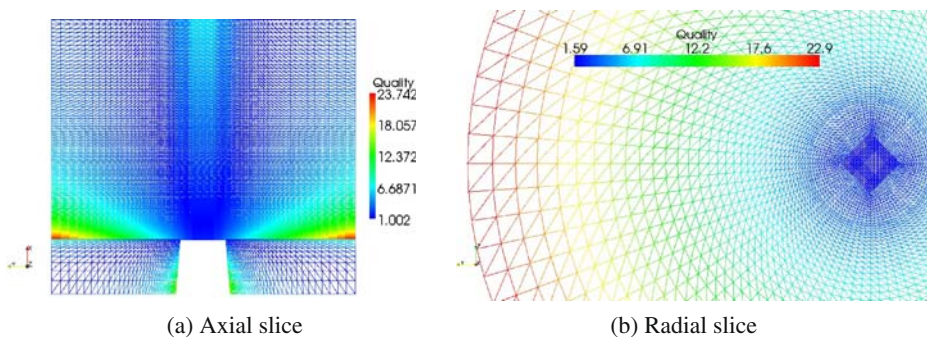


Fig. 11 Grid for simulation of isothermal and reacting flows. The quad elements are triangulated for visualization. The colors denote mesh quality based on edge length ratio. Best quality has value 1. **a** Axial slice. **b** Radial slice

The flashback simulation was started from the isothermal flow by igniting the mixture on the centerline at $2.4d_n$ above the nozzle. No attempt was made to model the ignition process in detail. The ignition was modeled by introducing artificial source terms into the progress variable transport equations, in the same way as it was already done in the combustion bomb test case above.

8 Results and Interpretation

8.1 Isothermal flow

For a successful modeling of the reacting flow during the flame flashback, it is essential that the isothermal flow is well reproduced by the numerical model described above. As a first step, Large-Eddy Simulations of the isothermal flow for the relevant flow configurations have been carried out.

Contour plots of the time-averaged isothermal axial velocity field for the LES and PIV measurements are compared in Fig. 12. Also, radial profiles of the axial velocity at selected axial stations are given in Fig. 13.

The same trend as reported in Section 4 can be observed in the numerical simulations: At $S = 0.43$ (case D9V20), a pronounced deceleration of the flow occurs above $x/D = 1.67$ near the axis. In spite of this, the flow does not reverse. For the lower swirl case D10V12, there is still a deceleration but it is rather mild.

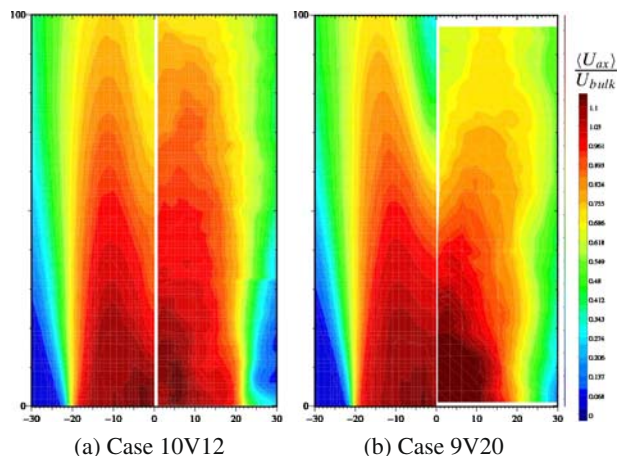
Compared to the measurements, the numerical simulation slightly overpredicts the strength of this flow deceleration. In general, the agreement between measured and computed velocity fields is acceptable.

8.2 Flame flashback

An overview of the simulations under investigation is given in Table 5.

For the evaluation of the results, at first the location of the flame tip is searched for each time step. The history of the flame tip distance from the swirler nozzle vs. time is shown in Fig. 14. Although the isothermal velocity field changes with increasing

Fig. 12 Comparison of measured and simulated isothermal velocity field. Left half of each contour plot shows LES result, right half shows PIV measurement. **a** Case 10V12. **b** Case 9V20



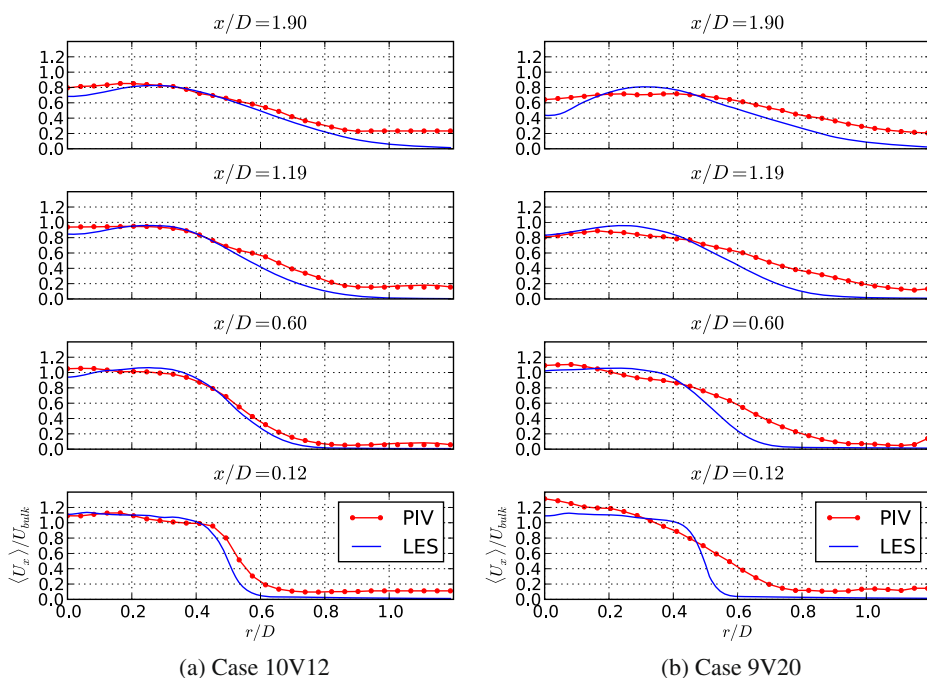


Fig. 13 Profiles of measured and simulated isothermal velocity field. Left half of each contour plot shows LES result, right half shows PIV measurement. **a** Case 10V12. **b** Case 9V20

distance from the swirler nozzle, the propagation velocity seems to remain constant in principle.

To give an impression of how the simulated flame propagation behaves compared to the experiments, experimental data is included in the figure. It is shown by the thin solid lines with bars in Fig. 14. These flame tip locations were evaluated from high speed video films. The bars show RMS in the flame tip location during the average over 30 runs each. Although the flashback is a stochastic event and only single incidents have been simulated it is compared to ensemble averaged experimental data. Ensemble averaging over a large number of simulations would be needed to draw a more meaningful conclusion, but this is unfeasible because of the too large computation time required on the hardware which was available to the authors. Furthermore, larger perturbations of the flow occurred in the experiments due to disturbances in the laboratory environment which were not present in the simulations and thus averaging of the experimental runs was required to gain useful data at all. Experiences with different simulations give rise to the assumption that the simulated flame propagation is much less fluctuating than the flame propagation in our experimental setup.

Table 5 Overview of performed simulations

Label	Swirl S	Volume flux \dot{V}	Fuel
10V12	0.34	$12\text{m}^3/\text{h}$	CH_4 ($\Phi = 1$)
9V20	0.43	$20\text{m}^3/\text{h}$	CH_4 ($\Phi = 1$)

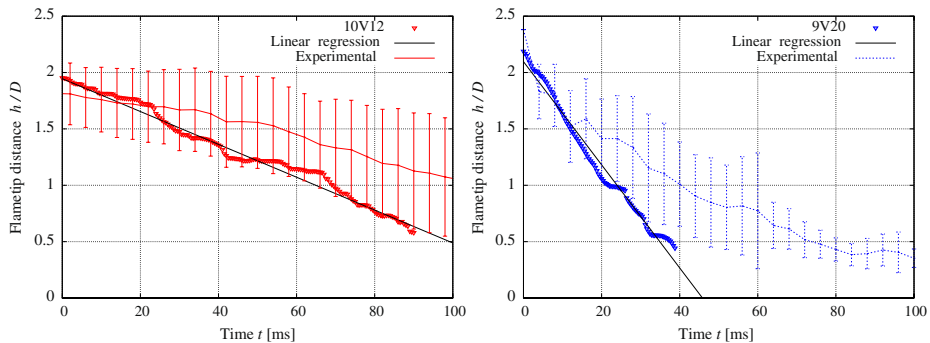


Fig. 14 Plots of flame tip to nozzle distance vs. time together with their linear regressions (*solid lines*). *Thin solid lines*: average over 30 experimental runs, the *bars* show RMS

It seems that the simulation overestimates the flame propagation speed but the agreement is regarded as acceptable because there is also uncertainty in the experimental boundary conditions and it is hard to quantify the influence on the propagation velocity. It is visible, that the observations reported in Section 4 are reproduced in the numerical simulation. From the linear regression analysis of the LES data, the flame propagation speeds can be estimated and are reported in Table 6.

To investigate the flow field in more detail, some kind of averaging is desired. Ensemble averaging is unfeasible but averaging in a flame tip fixed coordinate system is possible. That means, the time averaging is not done at fixed locations in space, i.e. cell centers in the space fixed computational grid, but at points that are fixed relative to the flame tip. The averaging is still done in time, so stationarity in this moving frame of reference is required. It does not strictly imply axisymmetry because no averaging over circumferential directions is included so far. Though, rotating or precessing structures would violate the assumption of stationarity. Furthermore, the velocity field and mixture properties should be homogeneous along the path of the flame for application of this averaging procedure. This is not strictly fulfilled in the current case, but the averaging is done this way nonetheless simply because not more data was available. It is therefore expected that the rendered picture is not sharp but rather blurred but still contains valuable information to get a deeper insight into physics of the process under consideration.

Technically, a cubical mesh, smaller than the entire domain, with a size of $4\text{cm} \times 4\text{cm} \times 4\text{cm}$ and a resolution $32 \times 32 \times 32$ cells was used for further analysis. For each time step, the center of this cube was shifted to the according flame tip location and all fields were mapped onto it. By doing so, the fields were spatially transformed into the moving flame tip fixed coordinate system and the amount of data was reduced to speed up subsequent computation of deduced quantities but time dependence was retained. All subsequent analyses were performed on this cutout. The flame tip fixed average could be computed simply as the time average over all cells of this grid.

Table 6 Flame propagation speeds from numerical simulations

Case	Propagation speed
10V12	$v_f = 0.61\text{m/s}$
9V20	$v_f = 1.92\text{m/s}$

If deduced quantities were to be evaluated, like vorticity or the vorticity production terms, they have been computed from the unaveraged raw data for each time step first and the result was then averaged afterwards.

The averaged velocity field for the two cases is shown in Fig. 15. The pictures show a slice through the mean velocity field together with a slightly transparent isosurface in the averaged temperature field. The latter gives an impression of the average flame surface shape. For the higher swirl case 9V20, the flame shape is conical and it is more spiky than for the lower swirl case 10V12. Furthermore, it is easily recognized that there exists a spot in front of the flame tip, where the axial velocity is strongly decelerated. In the high swirl case, the axial velocity even reverses its direction. It seems obvious, that the velocity in this region allows the flame to propagate against the main flow or even causes a convection of the reacting gases towards to swirler nozzle.

Since this spot is not present in the isothermal case, it must have been caused by the presence of the flame. As already argued in Section 1, this is a typical feature of vortex breakdown and vortex breakdown is connected to the creation of negative circumferential vorticity, i.e. a spiraling of the vortex lines. Figure 16 shows the vortex lines in the flame tip fixed averaged vorticity field for the two investigated cases. In both cases, the vortex lines are initially almost parallel but then spiral up significantly as they reach the flame front. In the 9V20 case the spiraling starts a little bit more ahead of the flame front than in the 10V12 case.

As already mentioned in Section 1, there is no common conception of whether the circumferential vorticity is created by radial expansion of the stream surfaces or a baroclinic mechanism. To learn more about the role of the different vorticity production mechanisms in the current case, the three production terms have been computed from simulation data. Figure 17 shows the probability density functions of the circumferential components of the production terms (see Fig. 2 for coordinate system conventions). What is remarkable is that all PDFs are slightly skewed towards production of negative circumferential vorticity. The baroclinic production term has

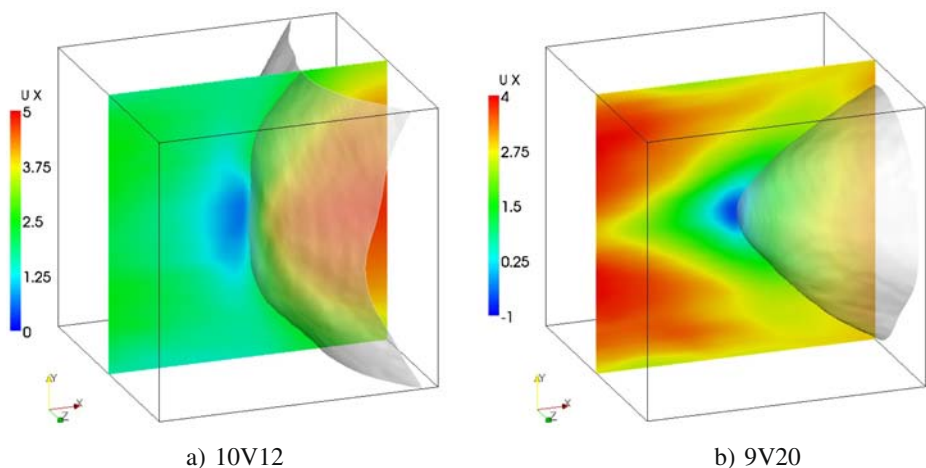


Fig. 15 Axial velocity field averaged in flame tip fixed coordinate system. Transparent surface: isosurface of averaged temperature $T = 1000\text{K}$. **a** 10V12. **b** 9V20

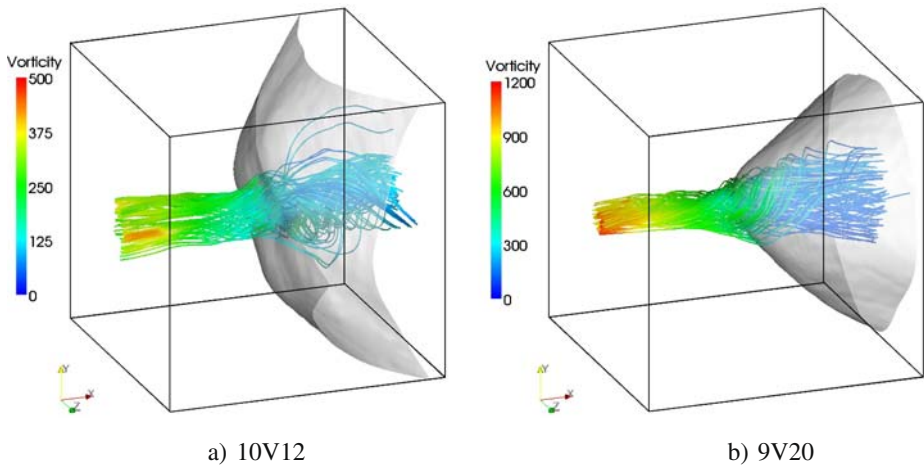


Fig. 16 Spiraling of vorticity lines at the flame front. Transparent surface: isosurface of averaged temperature $T = 1000K$. **a** 10V12. **b** 9V20

a high peak near zero and it is therefore most probable to find small values of baroclinic production.

For the low swirl case 10V12, the probability of the strain and dilution terms is almost symmetric between positive and negative branches. A more pronounced unsymmetry for these terms is found for the higher swirl case 9V20.

What is not visible from Fig. 17 is that at very large positive and negative values of the vorticity production, there is still a small but nonzero probability for the baroclinic production mechanism. This is probably attributed to a small number of very strong incidents like strong turbulent vortices interacting with the flame front. It remains unclear at this stage, whether this is also physically sound or merely a numerical issue.

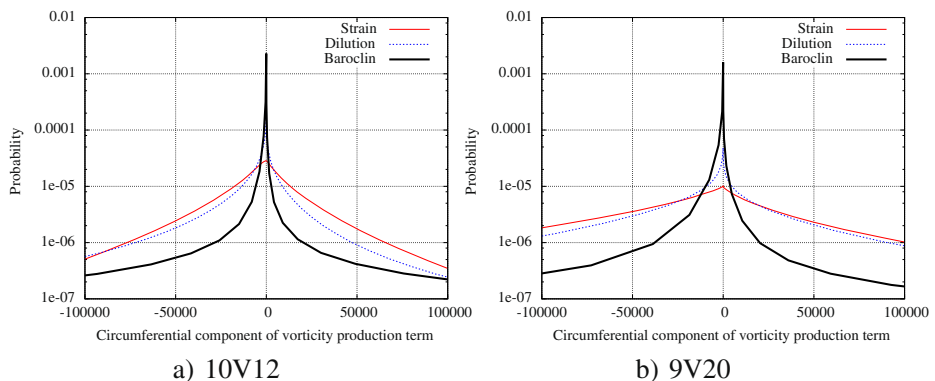


Fig. 17 Probability density functions of the circumferential components of the three different vorticity production terms. **a** 10V12. **b** 9V20

The vorticity does not act locally but induces a velocity in the whole domain according to Biot-Savarts law:

$$\mathbf{u}_{ind}(\mathbf{x}) = \frac{1}{4\pi} \int_{(V)} \frac{\boldsymbol{\omega}(\mathbf{x} - \mathbf{r}, t) \times (\mathbf{x} - \mathbf{r})}{|\mathbf{x} - \mathbf{r}|^3} dV \quad (30)$$

where \mathbf{x} determines the point where the velocity is calculated and \mathbf{r} is the radius vector of the elementary vortex. Differentiating (30) with respect to time and taking (2) into account we obtain the induced accelerations caused by the three different physical mechanisms:

$$\begin{aligned} \frac{d\mathbf{u}_{ind}}{dt} = & \frac{1}{4\pi} \int_{(V)} \frac{[-\boldsymbol{\omega}(\nabla \cdot \mathbf{u})] \times \mathbf{r}^*}{|\mathbf{r}^*|^3} dV \\ & + \frac{1}{4\pi} \int_{(V)} \frac{\left[\frac{1}{\rho^2} \nabla \rho \times \nabla p\right] \times \mathbf{r}^*}{|\mathbf{r}^*|^3} dV + \frac{1}{4\pi} \int_{(V)} \frac{[(\boldsymbol{\omega} \cdot \nabla) \mathbf{u}] \times \mathbf{r}^*}{|\mathbf{r}^*|^3} dV \end{aligned} \quad (31)$$

with $\mathbf{r}^* = \mathbf{x} - \mathbf{r}$.

Each component of the induced acceleration is now evaluated at a number of points along the vortex axis. The numerical computation of the Biot-Savart integrals is carried out using the method described in [3]. The result of integrating (31) is the axial distribution of the induced accelerations caused by the three different vorticity production mechanisms. The integration has again been done for the raw data of each time instant in the flame tip fixed coordinate system and the instantaneous axial profiles have been averaged in time afterwards. Thus, only quasi-steadiness of the induced accelerations was presumed and no kind of axisymmetry of the vorticity or its production terms.

The result is shown in Fig. 18 for the two cases. The bars in the figures show the RMS fluctuations of the induced accelerations. It is noticeable that the baroclinic source term shows very large fluctuations in both cases. The largest fluctuations appear around the flame tip, where the density gradient has the largest values.

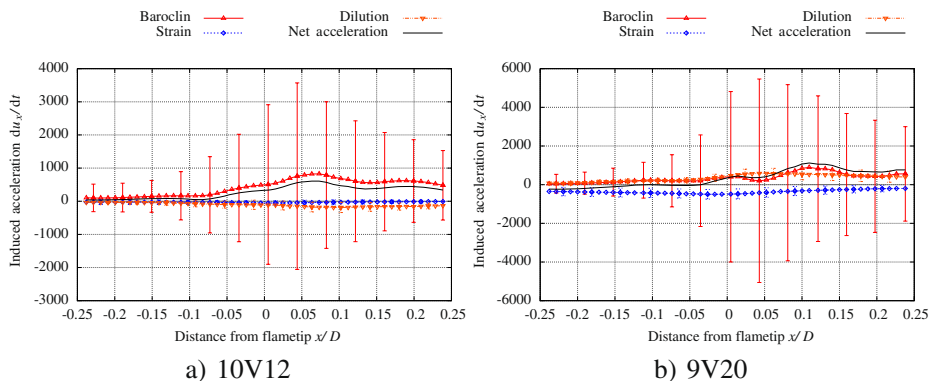


Fig. 18 Accelerations induced along the vortex centerline by the three different vorticity production terms, averaged in flame tip fixed coordinate system. Fresh gas is on the *left*, burnt gas on the *right*. The *bars* show RMS. Graphs of mean values without bars are shown in Fig. 19. **a** 10V12. **b** 9V20

This large fluctuations certainly arise from interactions of the pressure gradient in turbulent vortices with the flame front, which is characterized by a strong density gradient.

For the higher swirl case 9V20, the net acceleration is negative ahead of the flame tip. This means, that velocities against the main flow direction are induced and the flow is decelerated. As is apparent from Fig. 19 this is caused solely by the strain term, i.e. the widening of the stream surfaces due to the deflection of the streamlines. The volume expansion term counteracts the flame flashback as well as the baroclinic term does in the mean.

In the low swirl case 10V12, the net acceleration does not reach negative values anywhere in the considered cutout. It hardly reaches zero short distance ahead of the flame tip at the unburnt side. But as already expected from Fig. 15, the deceleration of the flow is not very strong in this case. The flow is decelerated but not enough to create a recirculation zone. It should be kept in mind that the presented figure relies only on a limited number of samples and induced accelerations are computed only along the centerline. But contrary to the 9V20 case, the flame is wider and events that influence the flashback are distributed over a wider space. Therefore, the conditions

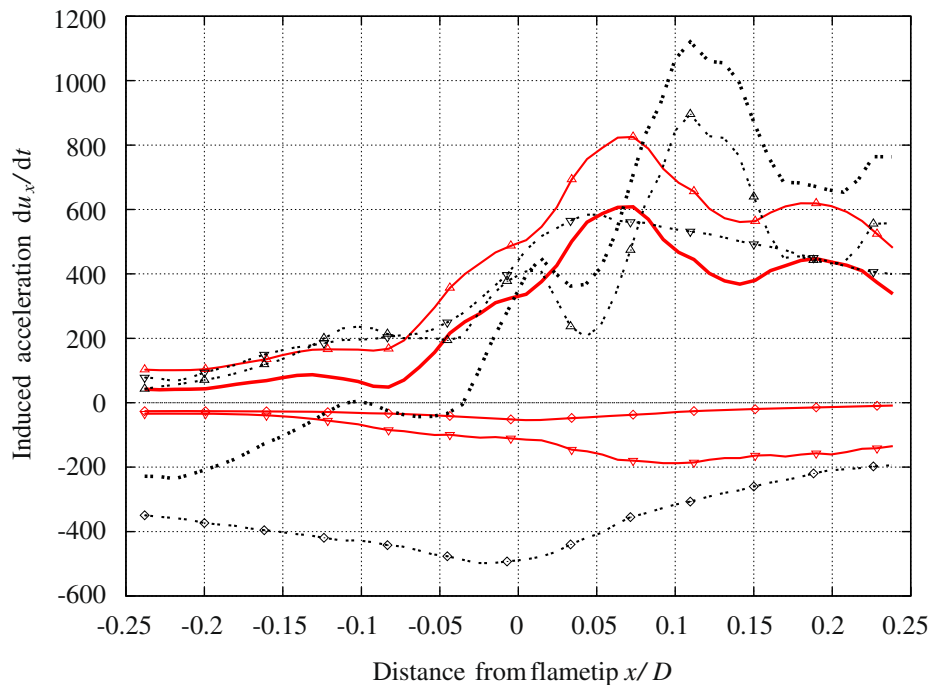


Fig. 19 Averaged accelerations induced along the vortex centerline by the strain and dilution production term, averaged in flame tip fixed coordinate system for both cases. Fresh gas is on the left, burnt gas on the right. Symbols denote different terms: Dilution (∇), Baroclin (Δ), Strain (\diamond), solid line: 10V12, dashed line: 9V20, thick lines: sum of all terms

for applying the averaging procedure are worse here. A more elaborated averaging would probably yield a figure with a very slight negative net acceleration for the 10V12 case. Anyway, it can be estimated that the strain and dilution term play a minor role in this case, but this cannot be clarified with the current analysis because of the uncertainties in the averaging procedure mentioned above.

9 Conclusion

Flame flashback in a free straight vortex has been studied experimentally and numerically. The vortex is steady, unconfined, fully turbulent and has a strong inner axial velocity.

Experimentally it was formed by a swirling jet of premixed methane/air and ejected into the ambient surrounding air by a movable block swirl generation device. The jet was ignited by an electrical spark and the flame propagation speeds have been measured using high speed video films. The isothermal flow has been measured by PIV method. Numerical simulations have been performed using LES with a presumed- PDF combustion model and ILDM chemistry model. The mathematical model was successfully validated for the isothermal flow under consideration, premixed turbulent combustion bomb and bunsen flame.

Investigations of the isothermal flow indicate no vortex breakdown inception at certain swirling numbers whereas clear flame flashback phenomenon takes place when the vortex is ignited. It points out that the negative velocities within the vortex jet provoking the flame flashback are determined by combustion process rather than by hydrodynamic isothermal effects related to the swirling jet destroy. Detailed LES analysis confirms that Combustion Induced Vortex Breakdown causes the flame flashbacks. At least for the higher swirl case, it was also shown that widening of the stream surfaces caused by the deflection of the flow by the flame causes a backflow region around the flame tip that sucks the reaction zone upstream. This study confirms the presence of the CIVB phenomenon in fully turbulent swirling jets.

Acknowledgements This work was done within the framework of the project HA2226/10-1 funded by the Deutsche Forschungsgemeinschaft (DFG). Some of the simulations were performed at the HLRN (High Performance Computing Center North). The HLRN service and support is gratefully acknowledged.

References

1. Ashurst, W.T.: Flame propagation along a vortex: the baroclinic push. *Combust. Sci. Technol.* **112**, 175–185 (1996)
2. Brown, G.L., Lopez, J.M.: Axisymmetric vortex breakdown part 2. Physical mechanisms. *J. Fluid Mech.* **221**, 553–576 (1990)

3. Carley, M.: Evaluation of biot-savart integrals on tetrahedral meshes. *SIAM J. Sci. Comput.* [arXiv:0712.1695v1\[math.NA\]](https://arxiv.org/abs/0712.1695v1) (2009)
4. Chen, Y.-C., Peters, N., Schneemann, G.A., Wruck, N., Renz, U., Mansour, M.S.: An experimental data set for turbulent premixed flames. <http://www.itv.rwth-aachen.de/index.php?id=84&L=0> (2007)
5. Chen, Y.-C., Peters, N., Schneemann, G.A., Wruck, N., Renz, U., Mansour, S.: The detailed flame structure of highly stretched turbulent premixed methane-air flames. *Combust. Flame* **107**, 223–244 (1996)
6. Chomiak, J.: Dissipation fluctuations and the structure and propagation of turbulent flames in premixed gases at high reynolds numbers. In: Sixteenth Symposium (International) on Combustion (1977)
7. Domingo, P., Vervisch, L.: Dns of partially premixed flame propagating in a turbulent rotating flow. In: *Proceedings of the Combustion Institute*, vol. 31, pp. 1657–1664 (2007)
8. Fiorina, B., Gicquel, O., Vervisch, L., Carpentier, S., Darabiha, N.: Approximating the chemical structure of partially premixed and diffusion counterflow flames using FPI flamelet tabulation. *Combust. Flame* **140**, 147–160 (2005)
9. Frenklach, M., Bowman, T., Smith, G., Gardiner, B.: Homepage of GRI-MECH reaction mechanism. http://www.me.berkeley.edu/gri_mech (2009)
10. Fritz, J.: *Flammenrückschlag durch verbrennungsinduziertes Wirbelaufplatzen*. PhD thesis, Technical University of Munich (2003)
11. Fritz, J., Kröner, M., Sattelmayer, T.: Flashback in a swirl burner with cylindrical premixing zone. *J. Eng. Gas Turbine Power* **126**(2), 276–283 (2004)
12. Goodwin, D.G.: *Cantera Users Guide*. Division of Engineering and Applied Science, California Institute of Technology, Pasadena, CA (2001)
13. Günther, R.: *Verbrennungen und Feuerungen*. Springer, Heidelberg (1984)
14. Hasegawa, T., Michikami, S., Nomura, T., Gotoh, D., Sato, T.: Flame development along a straight vortex. *Combust. Flame* **129**, 294–304 (2002)
15. Hasegawa, T., Nishikado, K.: Effect of density ratio on flame propagation along a vortex tube. In: *Twenty-Sixth Symposium (International) on Combustion*, pp. 291–297 (1996)
16. Herrmann, M.: *Numerical simulation of premixed turbulent combustion based on a level set flamelet model*. PhD thesis, RWTH Aachen (2001)
17. Hoffmann, A.: *Modellierung turbulenter Vormischverbrennung*. PhD thesis, Universität Karlsruhe (2004)
18. Issa, R.I., Ahmadi-Befrui, B., Beshay, K.R., Gosman, A.D.: Solution of the implicitly discretised reacting flow equations by operator-splitting. *J. Comput. Phys.* **93**, 388–410 (1991)
19. Kiesewetter, F.: *Modellierung des verbrennungsinduzierten Wirbelaufplatzens in Vormischbrennern*. PhD thesis, Technical University of Munich (2005)
20. Konle, M., Kiesewetter, F., Sattelmayer, T.: Simultaneous high repetition rate PIV–LIF-measurements of CIVB driven flashback. *Exp. Fluids* **44**, 529–538 (2008)
21. Kornev, N., Hassel, E.: Synthesis of homogeneous anisotropic divergence free turbulent fields with prescribed second-order statistics by vortex dipoles. *Phys. Fluids* **19**(5) (2007)
22. Kröger, H., Kornev, N., Wendig, D., Hassel, E.: Premixed flame propagation in a free straight vortex. *Forsch. Ing.wes.* **72**(2), 85–92 (2008)
23. Kröner, M.: *Einfluss lokaler Löschvorgänge auf den Flammenrückschlag durch verbrennungsinduziertes Wirbelaufplatzen*. PhD thesis, Technical University of Munich (2003)
24. Lopez, J.M.: Axisymmetric vortex breakdown part 1. Confined swirling flow. *J. Fluid Mech.* **221**, 533–552 (1990)
25. Maas, U., Bykov, V.: The extension of the ILDM concept to reaction-diffusion manifolds. *Combust. Theory Model.* **11**(6), 839–862 (2007)
26. Maas, U., Pope, S.B.: Simplifying chemical kinetics: intrinsic low-dimensional manifolds in composition space. *Combust. Flame* **88**, 239–264 (1992)
27. Nwagwe, I.K., Weller, H.G., Tabor, G.R., Gosman, A.D., Lawes, M., Sheppard, C.G.W., Wooley, R.: Measurements and large eddy simulations of turbulent premixed flame kernel growth. In: *Proceedings of the Combustion Institute*, vol. 28, pp. 59–65. The Combustion Institute, Pittsburgh (2000)
28. Pitsch, H., de Langeneste, L.D.: Large-eddy simulation of premixed turbulent combustion using a level-set approach. In: *Proceedings of the Combustion Institute*, vol. 29, pp. 2001–2008. The Combustion Institute, Pittsburgh (2002)
29. Poinot, T., Veynante, D.: *Theoretical and Numerical Combustion*. R.T. Edwards, Philadelphia (2005)

30. Umemura, A., Tomita, K.: Rapid flame propagation in a vortex tube in perspective of vortex breakdown phenomena. *Combust. Flame* **125**, 820–838 (2001)
31. van Oijen, J.: Flamelet-generated manifolds: development and application to premixed laminar flames. PhD thesis, Technical University Eindhoven (2002)
32. Weller, H.G., Tabor, G., Gosman, A.D., Fureby, C.: Application of a flame-wrinkling LES combustion model to a turbulent mixing layer. In: Twenty-Seventh Symposium (International) on Combustion, pp. 899–907. The Combustion Institute, Pittsburgh (1998)
33. Weller, H.G., Tabor, G.: Large eddy simulation of premixed turbulent combustion using Ξ flame surface wrinkling model. *Flow Turbul. Combust.* **72**(1), 1–27 (2004)
34. Weller, H.G., Tabor, G., Jasak, H., Fureby, C.: A tensorial approach to computational continuum mechanics using object orientated techniques. *Comput. Phys.* **12**(6), 620–631 (1998)